



Interfacial characterization of additively manufactured stainless steel to aluminium thin wall with nickel interlayer

Amrit Raj Paul^{1,2}, Manidipto Mukherjee^{1,2,a)} , Dilpreet Singh^{1,2}, Manas Kumar Mondal³

¹ CSIR-Central Mechanical Engineering Research Institute, Durgapur, West Bengal 713209, India

² Academy of Scientific and Innovative Research (AcSIR), Ghaziabad 201002, India

³ National Institute of Technology, Durgapur, West Bengal 713209, India

^{a)} Address all correspondence to this author. e-mail: m.mukherjee.ju@gmail.com

Received: 15 July 2022; accepted: 6 September 2022; published online: 13 September 2022

The formation of brittle incoherent Fe–Al intermetallics at dissimilar interface makes wire arc additive manufacturing (WAAM) of stainless steel (SS)–aluminium (Al) difficult. The incorporation of nickel (Ni) interlayers between SS and Al is thought to improve structural integrity. This article provides a detailed characterization of SS–Ni and Al–Ni interfaces. The Al–Ni interface is divided into three intermetallic zones: AlNi at center, Al₃Ni on Al side, and AlNi₃ on Ni side. The Ni₃Fe, NiFe, and NiFe₃ intermetallics at the SS–Ni interface increase with heat input. The intermetallics at the Al–Ni interface are found to be affected by heat input as well as primary dendrite arm spacing (PDAS) and dendrite growth angle (DGA) of the Ni dendrites. With low heat input, low DGA, and high PDAS, the intermetallic thickness at the Al–Ni interface decreases. It is also discovered that as heat input increases, the hardness of both interfaces increases.

Introduction

The wire arc additive manufacturing process (WAAM) is a versatile and economical [1] process with the ability to deposit small to large engineering components in comparison to the other metal additive manufacturing processes [2]. WAAM has been a center of attraction for researchers due to its highest deposition rate and less capital and operating cost among the different metal additive manufacturing processes. Till date, many researches have been published on the very common alloy system such as carbon steel [3], stainless steel [4], aluminium [5], copper [6], titanium [7], magnesium [8], superalloys [9], etc. Because of the large number of published studies on these alloy systems, the interest of the researchers has currently shifted towards the n-metallic ($n = 2, 3, 4, \dots$) functionally graded structures (FGS) from the single configuration alloy system. However, the various challenges associated with the dissimilar metal interface such as undesirable intermetallic formation, thermal stress-based cracking, inferior mechanical and metallurgical properties, etc., act as a backlash in the realization of such n-metallic FGS for the structural or functional application [10]. Despite the challenges, many researchers have successfully developed different FGS

with suitable metal combinations using WAAM. Tian et al. [11] deposited Ti–6Al–4V to AlSi₅ FGS through the WAAM process and found that the interface layers consist of continuous layers of intermetallics, Ti₇Al₃Si₁₂, and because of this, the failure occurred at the interface layer. A crack, of size ~ 40 μm, was observed at the interface layer which was initiated at the interface layer and propagated to the Al side under the residual stress due to the high difference in thermal conductivity and thermal coefficient of expansion. Marinelli et al. [12] deposited trimetallic FGS through the WAAM process with tantalum, molybdenum, and tungsten alloys and noticed a dense network of cracks at the interface between tantalum and molybdenum, however, no crack has been reported at the tungsten and molybdenum interface. This led to the knowledge that the intermediate alloys (as buffer layer) accommodate the residual stress and cyclical expansion with minimum localization of strain. Abe et al. [13] successfully deposited Ni6082 over SS308L and found that failure of the structure occurred at the Ni6082 side, not at the interface, which shows the excellent bond strength between the deposited dissimilar metallic structure. The diffusion was uniform in both of the metals and the interface width was ~ 200 μm. Shen et al. [14] deposited

Fe₃Al-based iron aluminide walls with 30 at.% Al content by using 99.5% pure iron wire and 1080 aluminium wire through the WAAM process. They noticed that the input current and interlayer temperature control the size of iron aluminides intermetallics in the process. In the literature survey, it was noticed that amongst all the deposited bimetallic or trimetallic FGS, the knowledge related to stainless steel (SS) and aluminium (Al) FGS is rare and dormant. The behaviour of the interface between these incompatible alloys with the deposition parameters is not known yet. However, the direct constitution of SS to Al interface through the WAAM process is very difficult due to its way apart physical, chemical, and thermal properties. The literature survey led to the understanding that the incompatible metals can be used to form FGS by the addition of an intermediate alloy matrix, especially, a soft alloy that can absorb residual stresses and cyclic deformation [15, 16]. Therefore, in this work, the deposition of SS and Al with Ni interlayer layer between the two has been realized by using the WAAM process. Adding a few layers of high-nickel-based alloy in between the stainless steel and aluminium may lead to the formation of SS–Ni–Al FGS with two metallic interfaces; stainless steel–nickel (SS–Ni) interface and nickel–aluminium (Al–Ni) interface. Nonetheless, the possibility of the formation of compatible intermetallics sequence at the Al–Ni interface is extremely high, which could lead to the structural integrity of the deposited SS–Ni–Al structure. In this context, detailed characterization of the SS–Ni and Al–Ni interfaces is required to analyse the metallurgical and mechanical behaviour of the Al–Ni and Ni–Fe intermetallics formed at the Al–Ni and Ni–SS interfaces, respectively. The successful fabrication of SS–Al FGS with Ni interlayer structure may open a gateway for the manufacturing of SS–Al dissimilar structural and functional components with near net shape features by using the WAAM process. This work aims to provide detailed information on microstructural features and the hardness of Al–Ni and Ni–Fe interfaces. This will add clarity to the Al–Ni and Ni–Fe dissimilar interfaces in terms of intermetallics formation behaviour and their effect on the structural integrity for the fabrication of SS–Ni–Al trimetallic structures by using the WAAM process. Out of the 25 sets of miniature SS–Ni–Al walls with heights of 30 mm and lengths of 50 mm, four walls were chosen for detailed microstructural and hardness characterization. These 25 sets of walls were fabricated using the design of experiment (DoE) with an L25 orthogonal array having two factors, i.e., mean input current (I_m) and deposition speed (DS), and five levels. According to the increasing order of heat input, all four selected samples have Al–Ni and SS–Ni interfaces denoted as AN1, AN2, AN3, & AN4, and NS1, NS2, NS3, & NS4 respectively. A detailed characterization of the behaviour of intermetallics with varying heat input has been carried out at these

two interfaces. Furthermore, various hypothetical models illustrating the intermetallics formation mechanism et al.-Ni and SS–Ni interfaces have been developed to close the knowledge gap on the topic.

Result and discussion

Optical microscopy of SS–Ni and Al–Ni interfaces

Figure 1 illustrates optical microscopic images of selected samples with microstructural variations across the two interfaces. The SS region below the SS–Ni interface is generally composed of the primary austenite matrix and high-temperature δ -ferrite segregated at the austenitic grain boundary. The Ni region above the SS–Ni interface contains the dendritic gamma (γ) phase and the gamma prime (γ') segregated at the interdendritic region. The formation of intermetallic compounds (IMC) of Fe–Ni may occur throughout the transition between SS and Ni. Since Fe–Ni IMCs are primarily face-centered cubic (FCC) structures, they should be ductile and tough enough to provide superior integrity of the interface without any defects [10]. However, the Fe–Ni intermetallic thickness (IMT) varies from 10.23 to 26.82 μm as the input parameters are changed. Since the WAAM process has a very fast cooling rate (a few seconds), solid-state diffusion of Fe and Ni atoms within the matrix is negligible [3, 17] and the formation of Fe–Ni IMCs should have occurred primarily in the liquid state, through the mixing of two molten metals. The preceding statement is validated by comparing the interlayer cooling time (Δt) and the time required to form the specific thickness of Fe–Ni IMC at the interface. The Δt from 1455 °C (T_1) to 800 °C (T_2) for the Ni6025 layer was calculated by using the Eq. 1 [18].

$$\Delta t = \frac{1}{4\pi k \rho c} \left[\frac{1}{(T_2 - T_0)^2} - \frac{1}{(T_1 - T_0)^2} \right] \left[\frac{\eta VI}{Sd} \right]^2 \quad (1)$$

where Δt is the time required to reach from temperature T_1 to T_2 , k is the thermal conductivity (W/mm/°C), ρ is the density (Kg/mm³), c is the specific heat (J/Kg/°C), T_0 is the Room temperature (°C), T_1 is the Melting point (°C), T_2 is the transformation temperature (°C), η is the arc efficiency (85%), V is the input voltage (volts), I_m is the input current (ampere), S is the deposition speed (DS) (mm/s) and d is the interfacial layer height (mm). The d values of NS1, NS2, NS3, and NS4 were 2.5 mm, 2.63 mm, 2.81 mm and 2.96 mm respectively. The thermal conductivity ($k = 0.04$ W/mm/°C) and heat capacity ($\rho c = 0.005$ J/mm³/°C) values were taken for nickel alloys from reference [18]. The Δt of the SS–Ni interfaces was calculated as 3.02 s, 23.5 s, 25 s, and 33.83 s for NS1, NS2, NS3, and NS4, respectively.

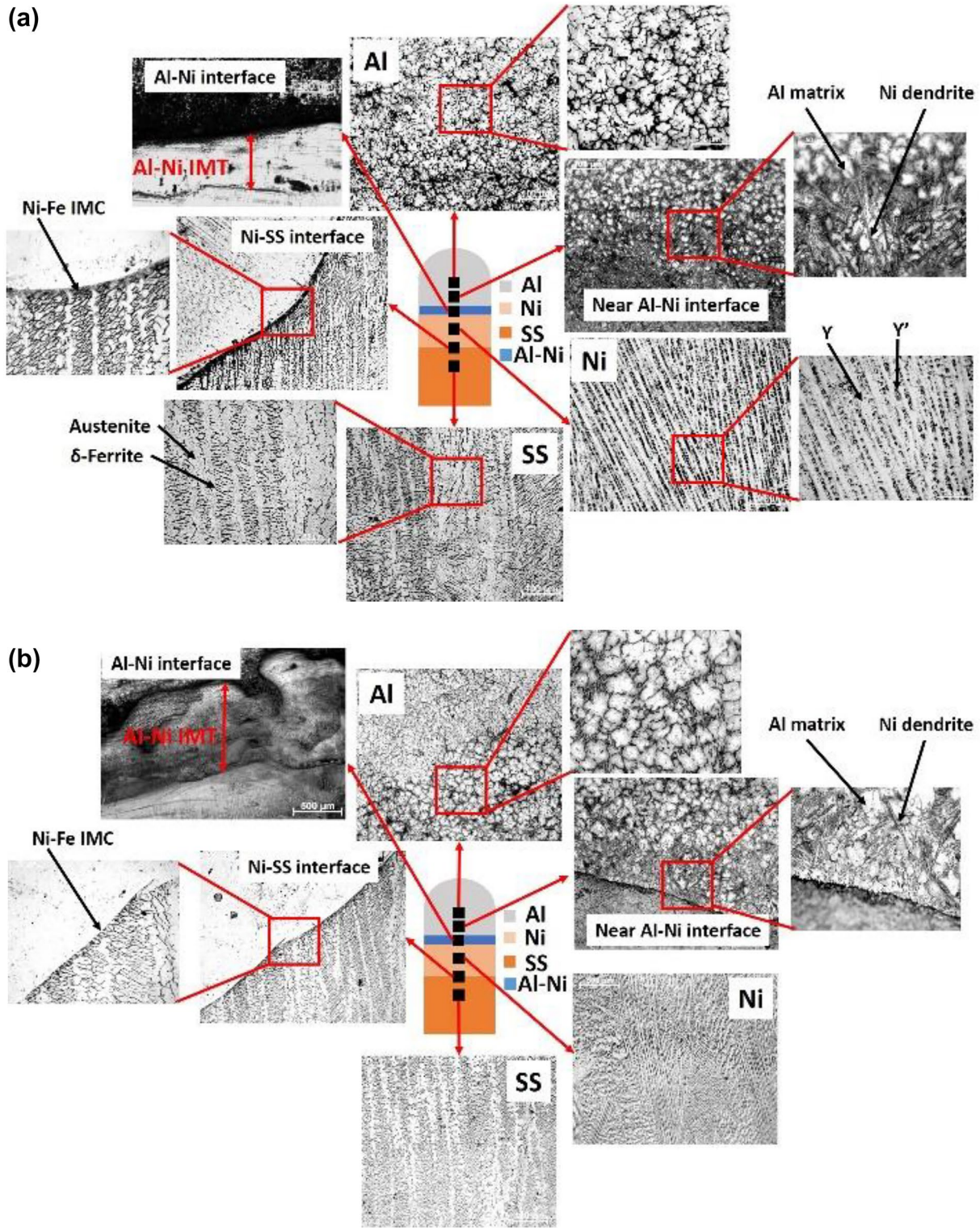


Figure 1: Optical micrographs of SS–Ni and Al–Ni IMC zones (a) NS1/AN1, (b) NS3/AN4, (c) NS2/AN2, and (d) NS4/AN3.

The time required to form the specific thickness of Fe–Ni IMC at the interface can be calculated from Fick’s second law where the concentration gradient of solid-state diffusing of material can be

described by the Eq. 2 [19]. Where, C_s is the constant concentration of the diffusing atoms at the surface of the material, C_0 is the initial concentration of the diffusing atoms in the material and C_x

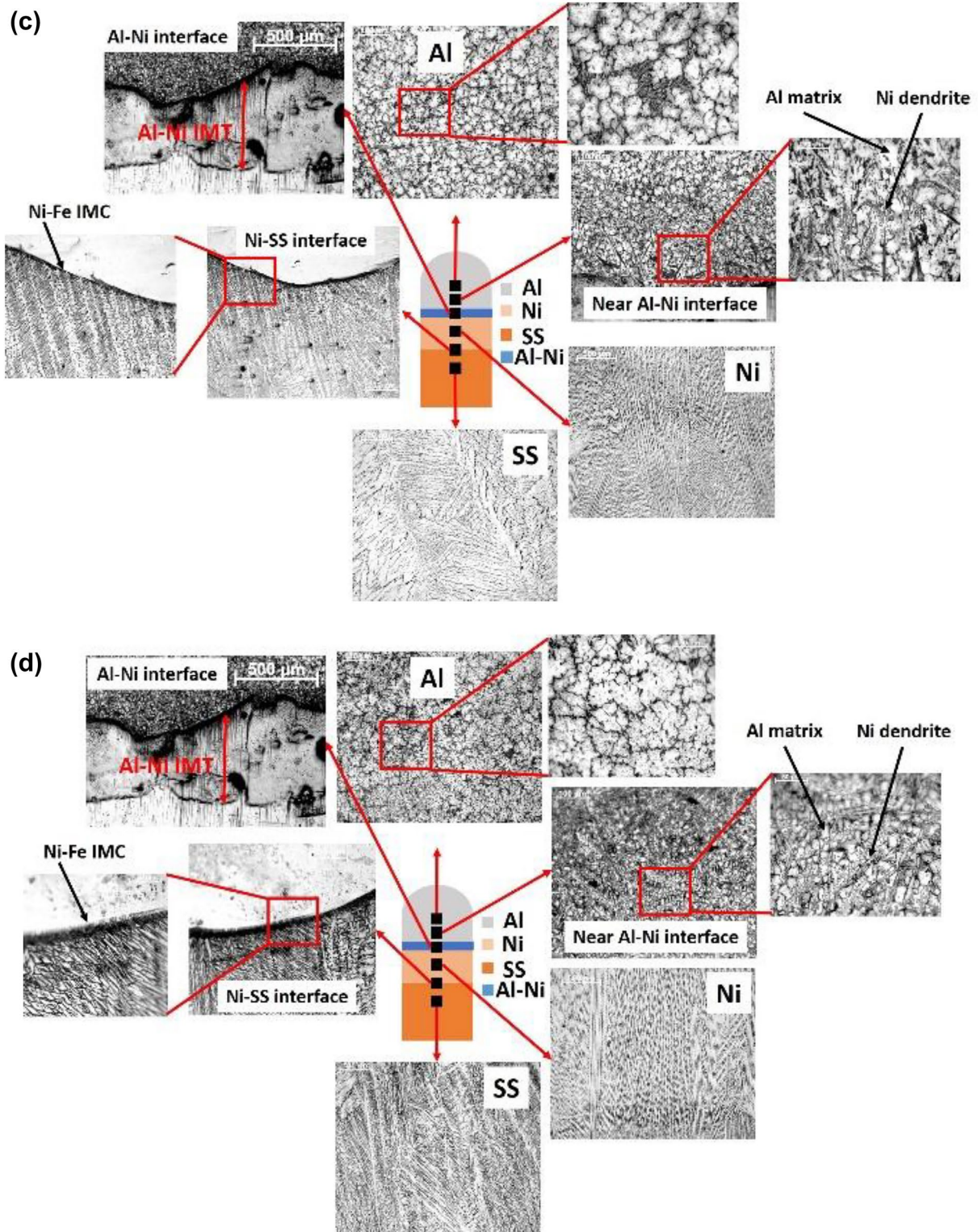


Figure 1: (continued)

is the concentration of diffusing atom at the location x below the surface after time t .

$$\frac{C_s - C_x}{C_s - C_0} = \operatorname{erf}\left(\frac{x}{2\sqrt{Dt}}\right) \quad (2)$$

The average of T_1 and T_2 is taken for solid-state diffusion (1127.5 °C) at the SS–Ni interface. Here it is assumed that the Ni and Fe equally diffuse into each other, and the Ni–Fe IMT has half part on the Ni side and another half part on the SS side. Among the NS1, NS2, NS3, and NS4, the NS3 has a minimum Ni–Fe IMT of 10.42 μm (Table ST1), which is selected to calculate the minimum time taken by solid-state diffusion to form 5.21 μm of IMT at both Ni and SS side. The different parameters used to calculate the time are given in supplementary Table ST2 [19].

The diffusion coefficient (D) is calculated by the following equation [19]. Here, Q is the activation energy (J/mol), R is the universal gas constant (8.314 J/mol/K), T is the temperature and D_0 is the diffusivity constant.

$$D = D_0 e^{-\frac{Q}{RT}} \quad (3)$$

The time calculated for the diffusion of Fe into Ni for 5.21 μm is ~ 5000 s and that is of Ni into Fe for the same thickness is ~ 280 s. Therefore, the overall time taken for the solid-state diffusion to develop 10.42 μm of Ni–Fe IMC is extensively high in comparison to the Δt value of 25 s. Thus, the mechanism of intermetallic formation at the SS–Ni interface is primarily caused by the mixing of elements in the molten state. The optical micrographs further reveal the formation of a thick Al–Ni IMC layer at the Al–Ni interface along with the growth of Ni dendrites in the Al matrix near the interface. This implies that the Ni layer is partially melted during the subsequent deposition of the Al layer, and Ni dendrites grow in molten Al during solidification. The solidification of Al–Ni interface is much faster than the SS–Ni interface due to very high thermal conductivity of aluminium. Furthermore, the diffusivity constant (D_0) of Al in Ni is around $4.5 \times 10^{-6} \text{ m}^2/\text{s}$ [19], which leads to the very slow solid-state diffusion of Al in Ni matrix. In addition, the large gap between the atomic radius of Al (143 pm) and Ni (124 pm) [19] consequently hurdle the solid-state movement of Ni atom in Al matrix. Therefore, similar to the SS–Ni interface, the IMCs at Al–Ni interface also formed by the mixing elements at liquid state before solidification instead of solid-state diffusion. However, optical microscopy does not reveal the mixing mechanism at the SS–Ni and Al–Ni interfaces. Therefore, scanning electron microscopy (SEM) and energy dispersive X-ray spectroscopy are used to reveal the mechanisms.

Scanning electron microscopy (SEM) & Energy dispersive X-ray spectroscopy (EDS) of SS–Ni and Al–Ni interfaces

SS–Ni interface

The SEM analysis of SS–Ni interfaces are investigated thoroughly and found that the hypothesis developed by optical microscopy is justified. The NS1 sample has lowest heat input (~ 200 J/mm) leads to supercooling of the weld pool (~ 3 s) resulting in solidification of the Ni embryo in the Fe matrix [Fig. 2(a)]. The SEM images of the SS–Ni interface revealed that SS–Ni mixing zone appeared in NS2 and NS3 samples because of the two times higher heat input (NS2 = ~ 558 J/mm and NS3 = ~ 576 J/mm) than NS1 which provides relatively slower cooling and adequate time to the formation of Ni–Fe IMC [Fig. 2(b) and (c)]. The NS4 sample experienced maximum heat input (~ 670 J/mm) resulting in the formation of thicker IMC than the NS2 and NS3 samples with Fe and Ni solid solutions zone at the SS–Ni interface [Fig. 2(d)]. Surface tension force, buoyancy force, and electromagnetic force can be used to describe the mixing of elements in the molten pool during the WAAM process [Fig. 2(e)]. Surface tension and buoyancy forces act outward from the middle along the liquid interface, whereas the electromagnetic force is acting downward along the central axis. The simultaneous interaction of these forces causes turbulence in the molten pool, allowing elements to mix. However, this mechanism is only valid for metals with similar physical and chemical properties, such as Fe and Ni. During the mixing process, the concentration of Ni and Fe reaches to a stoichiometric and favorable condition to form different Ni–Fe IMC at the SS–Ni interface [Fig. 2(f)]. The formation of Ni–Fe IMC, solid solution and the size of mixed zone at the SS–Ni interface is summarized in supplementary Table ST3.

However, the type of intermetallics formed at the SS–Ni interface with varying input is assessed by the EDS analysis as shown in Fig. 3. The results of NS1 sample clearly shows that the atomic percentage of Ni and Fe at the interface is ~ 6 –8% and ~ 21 –28% respectively [Fig. 3(a)] which suggests large solid solution of Fe in Ni leading to almost uniform distribution of Fe along the interface creating NiFe_3 type of IMC. The NiFe_3 IMC is generally a metastable phase because of its positive enthalpy of formation (2.731 kJ/mol) [10]. The positive enthalpy of NiFe_3 formation causes liberation of heat, which further contributed to the widening of the mixed region at the SS–Ni interface of the NS1 sample. However, in the current study, the NiFe_3 phase has been stabilized at room temperature, probably due to the presence of significant Ni content in the nearby matrix.

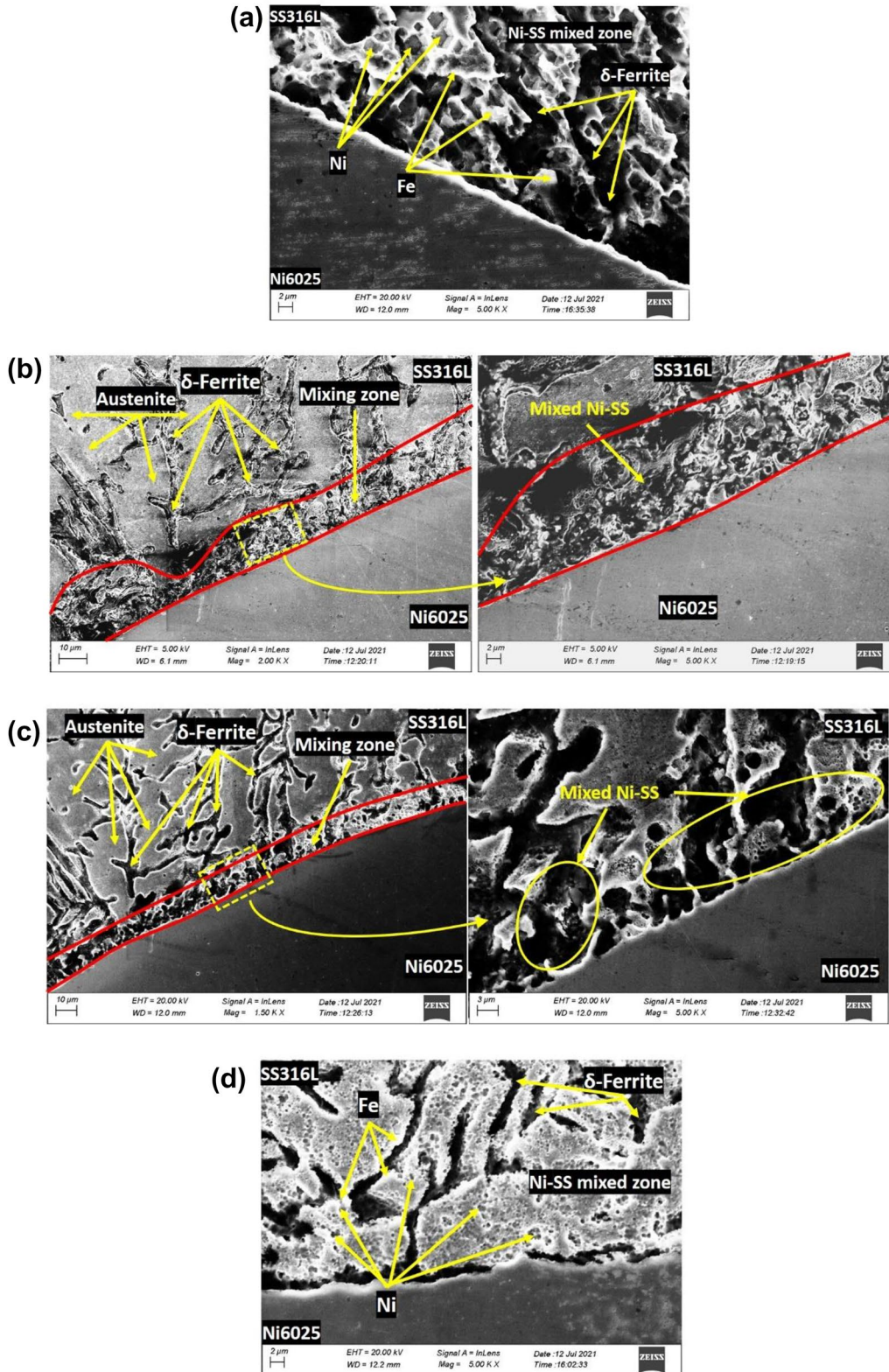


Figure 2: SEM images of the SS–Ni interface for (a) NS1, (b) NS2, (c) NS3, (d) NS4, (e) Different forces acting in the molten metal pool during WAAM process, and (f) Mixing process of Ni6025 and SS316L during WAAM process.

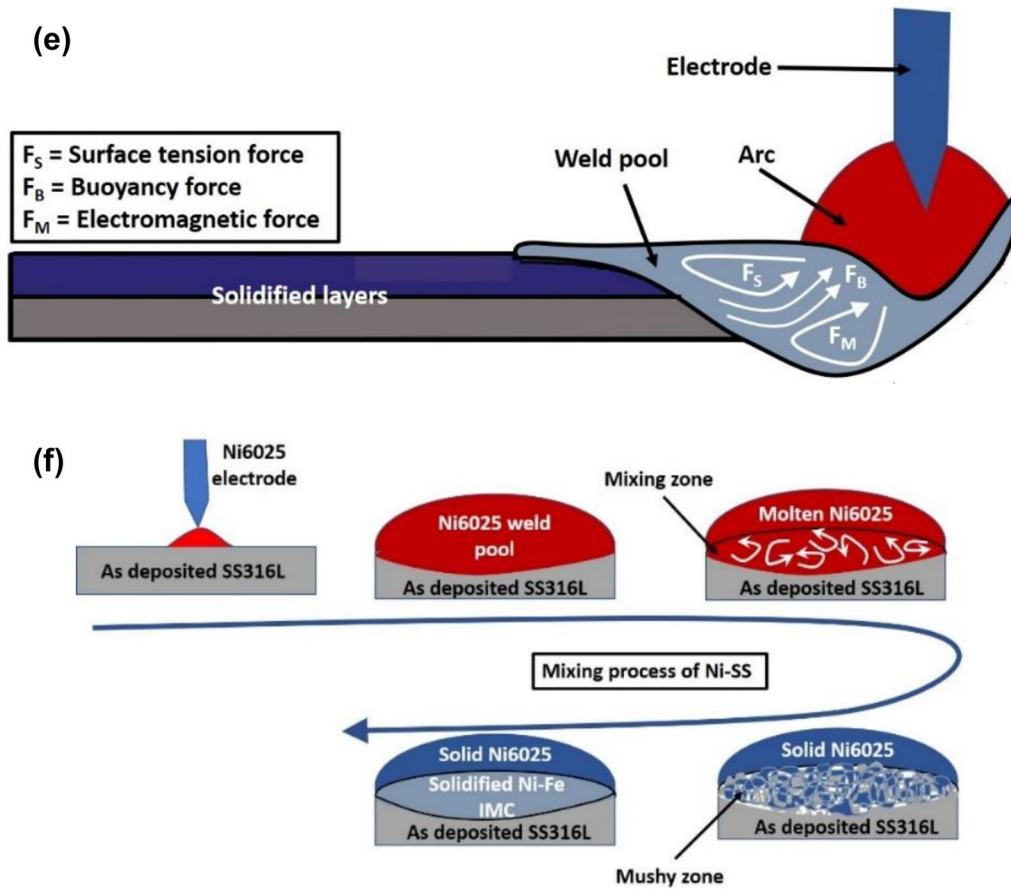


Figure 2: (continued)

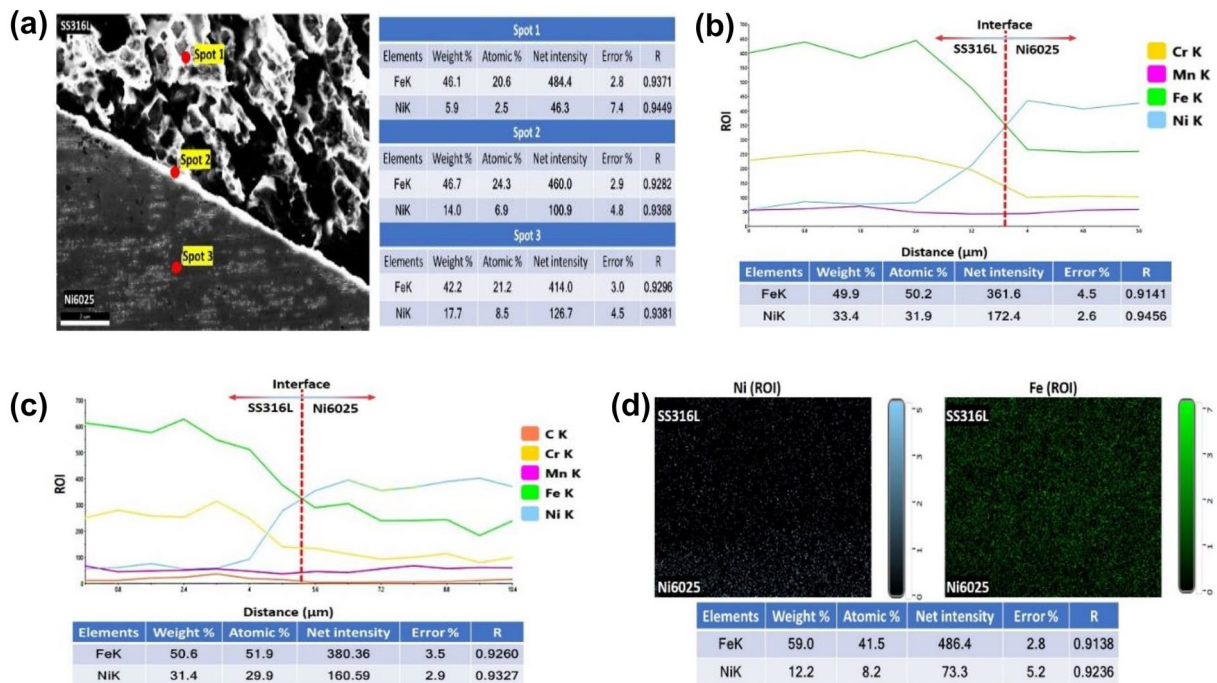
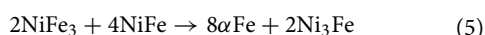
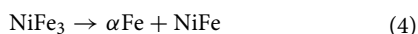


Figure 3: EDS analysis of SS–Ni interfaces (a) point scan of NS1, (b) line scan of NS2, (c) line scan of NS3 and (d) area scan of NS4.

Because the heat input for samples NS2 and NS3 is nearly identical, the elemental distributions of both samples are similar, as shown in Fig. 3(b) and (c). It is observed that the atomic percentage of Ni and Fe for both of samples lies in the range of 18–31% and 26–50% respectively indicating the formation of equiatomic NiFe and Ni₃Fe IMCs. The slow cooling rate associated with higher heat input in NS2 and NS3 probably leading to the transformation of NiFe₃ into NiFe [10]. However, NiFe phase is also metastable and further transformed into Ni₃Fe during cooling. The transformation kinetics of the same can be understood by the following reactions.



The NS4 sample is having the maximum heat input among the selected samples (NS1, NS2, NS3 and NS4) which also leads to the partial transformation of NiFe into Ni₃Fe [Fig. 3(d)]. The formation of solid solution is preferred in the mixing zone of NS4 along with large fraction of retained NiFe and small fraction of Ni₃Fe. It is possible to postulate from the EDS analysis that the fraction of Fe–Ni IMCs across the interface increases with increasing heat input, but large high heat input results in an excessively large solid solution of Fe and Ni which reduces the tendency of phase transformation (supplementary Table ST4).

Al–Ni interface

The SEM images of Al–Ni interfaces [Fig. 4] supports the same theory that has been discussed in “Optical microscopy of SS–Ni and Al–Ni interfaces” section (prominent mixing than diffusion). Partial melting of the Ni6025 layer at the Al–Ni interface occurred because of two types of thermal associations during the deposition of Al4043 layer. The first is direct heat generated by the arc during deposition, and the second is convective heat transfer through interface from molten Al4043. The liquid Al and Ni are mixed together under the active forces acting in the molten pool in the same way as shown in Fig. 3(f). The presence of thick continuous layer at the Al–Ni interface is confirmed by microscopy [Fig. 4] due to direct mixing of Al and Ni. Interestingly, the thick layer of IMC at the Al–Ni interface is actually divided into two new interfaces. The IMC–Ni and the IMC–Al interfaces have been observed around the central Al–Ni IMC zone. The IMC–Al zone has less nickel content than the central IMC zone. The nickel solidifies first at the IMC–Al zone as a dendrite and then grows into the liquid Al. As shown in Fig. 4, the heterogeneous nucleation of aluminium began around solidified nickel dendrites during the continuous cooling of the deposited layer. The AN1 sample is having the lowest heat input (~ 40 J/mm) and hence, the Ni has very less time to penetrate and grow

into the Al resulting in thinnest Al–Ni IMC. Moreover, due to rapid cooling of AN1, the Ni dendrites are also broken into small pieces, as shown in Fig. 4(a). The similar phase formation behaviour has been also observed at the IMC–Al interface of AN2, AN3 and AN4 samples, as depicted in Fig. 4(b–d), respectively. Based on the obtained results, the entire solidification and phase formation behaviour of Ni into Al at the IMC–Al zone is described by a schematic model [Fig. 4e], where the following sequential steps may occur.

Ni-dendrite + L–Al → Ni-dendrite growth + Al-embryo + semisolid Al

Ni-dendrite + Al grains

The growth of Ni dendrite and Al grains is affected by heat input. Fig. 4 shows that as the heat input of the samples increases both the thickness of Ni dendrites and the growth of Al, surrounding the dendrites, increases. However, the Al–Ni intermetallic thickness (IMT) of samples [Fig. 1] is not only governed by heat input, but also dependent on the combined effect of PDAS and dendritic growth angle (DGA) of Ni (with respect to the horizontal direction). The penetration of Ni dendrite in the Al matrix increases with higher DGA and lower PDAS values of Ni. As a result, the higher PDAS and lower DGA produces thinner Al–Ni IMC layer as illustrated in Fig. 4(f). For example, the AN3 sample experienced slightly higher heat input (~ 70 J/mm) than the AN2 sample (~ 65 J/mm) during Al layer deposition, but nevertheless showed lower IMT due to higher PDAS and lower DGA values than the AN2 sample. The PDAS value of AN2 is 4.1 μm smaller than the AN3, because of higher heat input, but the DGA value of AN2 is ~ 75.11° which is ~ 5° bigger than the AN3. The lower DGA of AN3 sample may create additional resistance to the growth of Ni in the Al matrix resulting in lower IMT. Among all the interfaces, the AN4 experienced highest heat input (~ 80 J/mm) with PDAS and DGA values of 15 μm and 86°, respectively, resulting in the highest Al–Ni IMT [Fig. 4(f)]. Looking towards the Ni side of the Al–Ni IMC layer, a mixed Ni-rich and Al-deficit region is noticed near the IMC–Ni interface as shown in Fig. 5(a) and (b). It is observed that the Al is present in this zone as a form of band, which indicates different kind of mixing mechanism than the IMC–Al interface. The mechanism that created band formation is the stretching and folding of Al layer followed by prior diffusion [20] as illustrated in Fig. 5(c). This process typically occurs during the dissimilar autogenous fusion welding of materials with large melting point differences, such as Al and Ni in this study. High melting point materials like Ni generally melts partially during the fusion process because of the direct heating by arc energy and convective heat from the molten low-temperature material (Al). The forces acting in the molten pool [Fig. 2(f)] create a vortex-like structure and forced the Al into the partially melted Ni region. These vortex-like structures have previously been

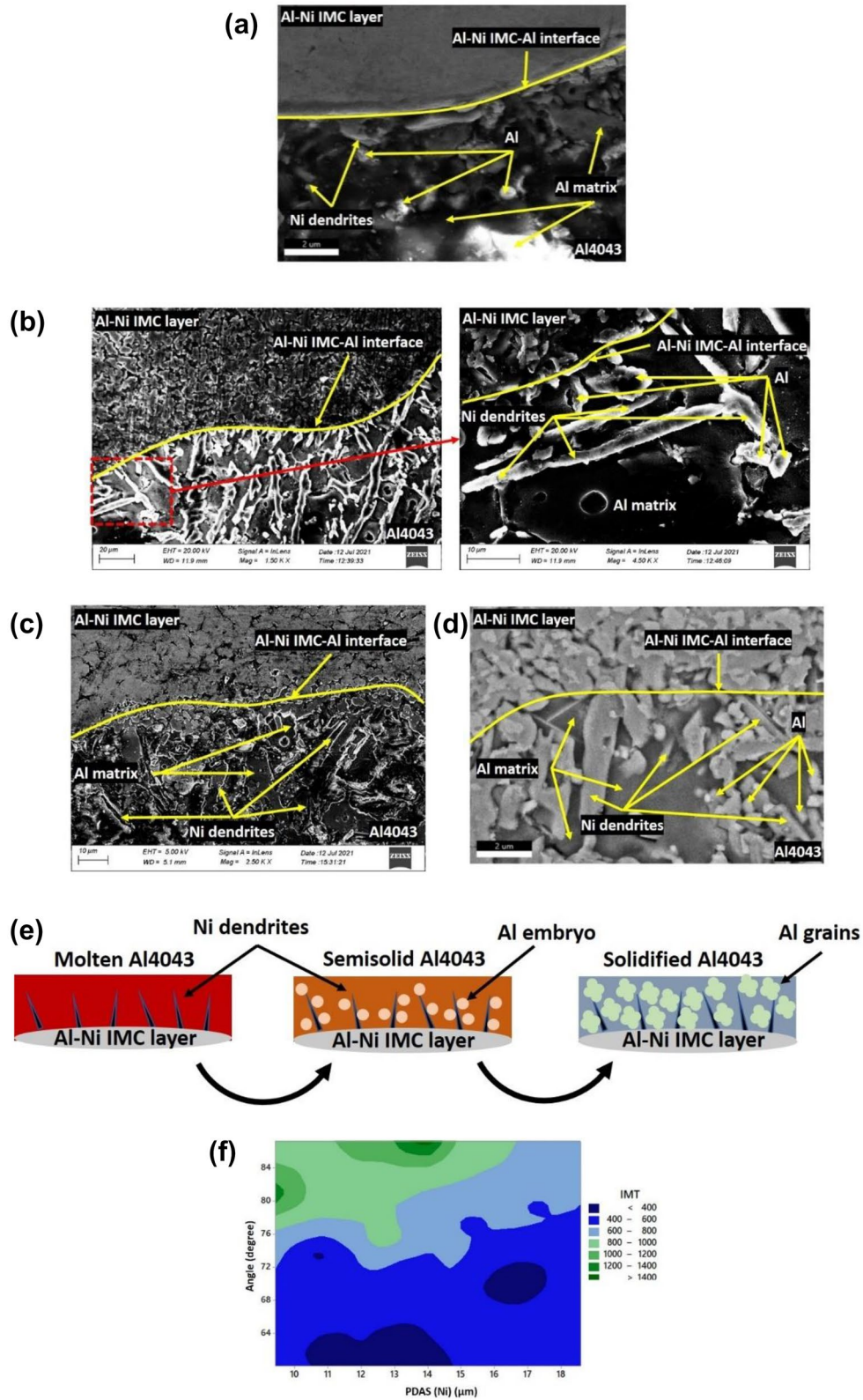


Figure 4: SEM images of Al–Ni IMC–Al interface for (a) AN1, (b) AN2, (c) AN3, and (d) AN4, (e) Solidification behaviour of Ni into Al at Ni deficient region (f) Variation of IMT with respect to PDAS and DGA.

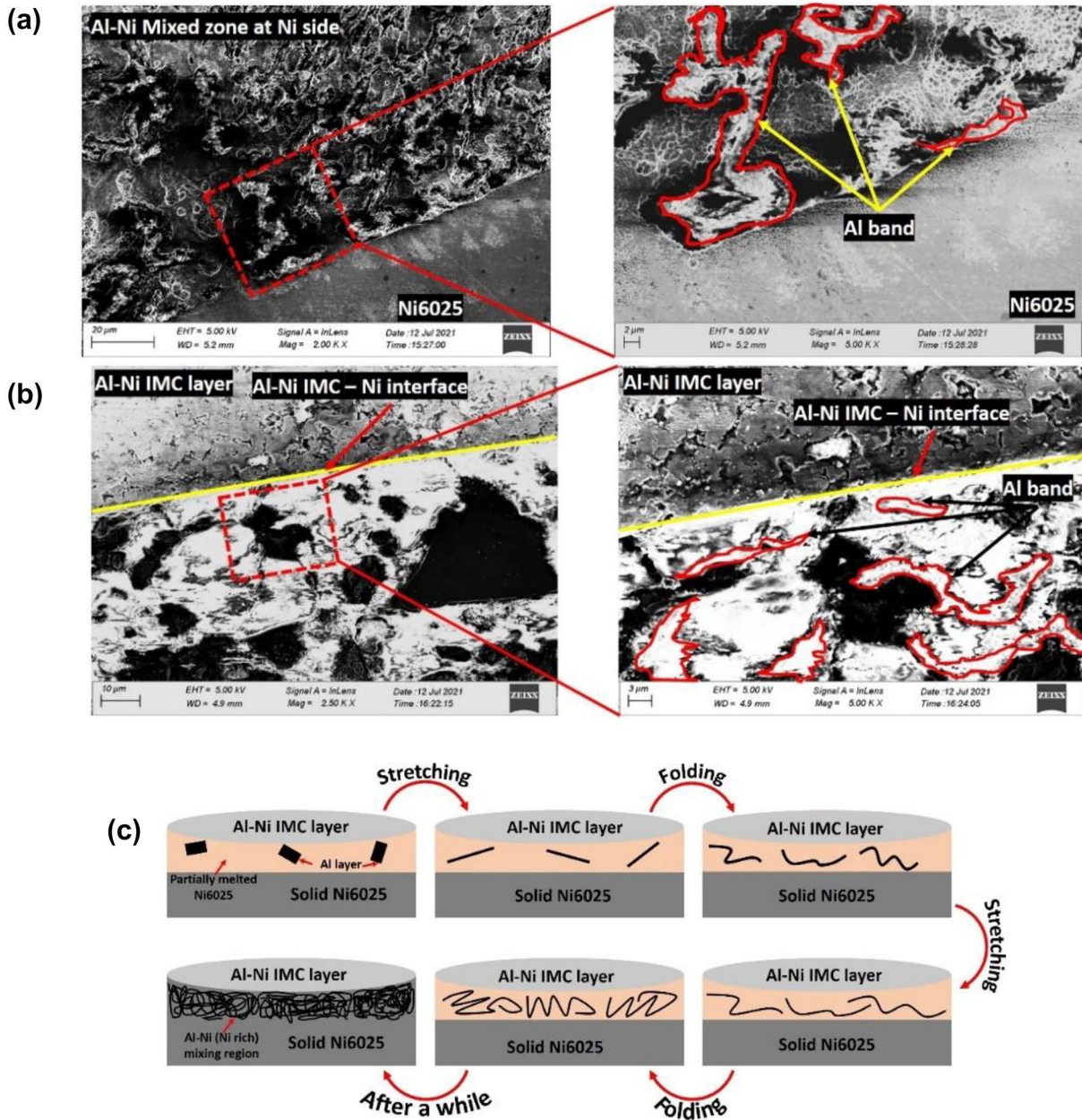


Figure 5: Al-Ni IMC-Ni mixed zone for (a) minimum heat input (AN1), and (b) maximum heat input (AN4), (c) Mixing mechanism of Al and Ni rich regions.

observed in dissimilar welding of Ni-Cu [21] and Ni-Fe [22] fusion welding processes which also created band-like microstructure at the dissimilar interfaces. The mixing of Al into Ni is influenced by the relative conductivity of the two participating materials as well as the heat input and melting point of the two materials. The large thermal conductivity difference between Al and Ni limits Al fluid motion into Ni, as evidenced by the EDS results, which show only 25% Al penetrated into the Ni region. The small amount of Al that is stretched by the change in force dynamics in the melt pool also experience

abrupt bending. The thickness of Al bands is reduced after each stretching and bending until it is small enough to allow diffusion between the elements (Al and Ni) and favor the formation of IMCs as discontinuous precipitates [Fig. 5(c)].

The total Al-Ni IMC layer may be divided into three distinct IMC regions according to the phase formation and solidification behaviour. The central region with an equal proportion of Al and Ni, i.e., a 50:50 ratio, could lead to the formation of AlNi. The IMC-Al interface region is high in Al content, which could lead to the formation of Al-rich IMCs

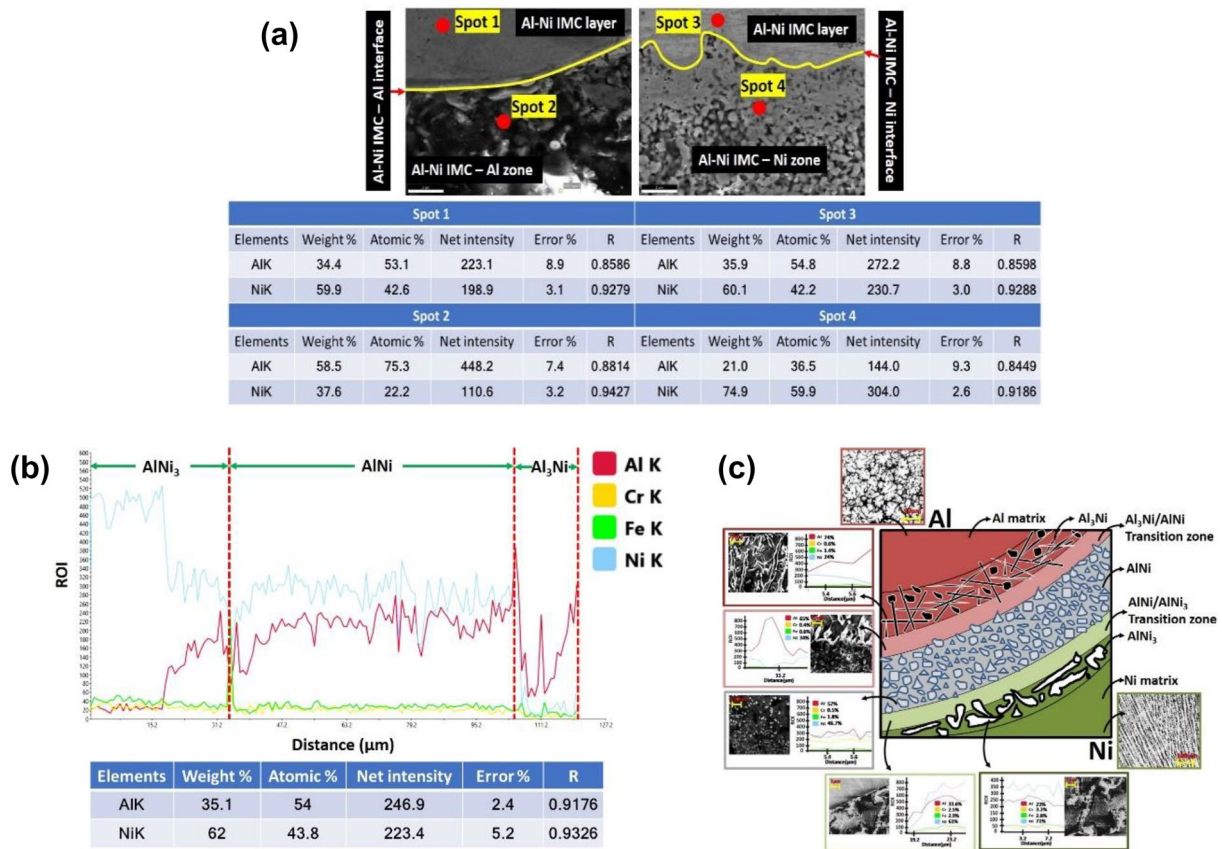
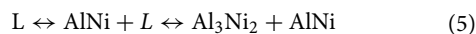
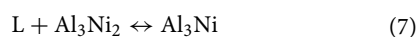


Figure 6: EDS analysis at Al-Ni interface for sample AN1 (a) Point scan, (b) Line scan, (c) Schematic model for phase formation across the Al-Ni interface.

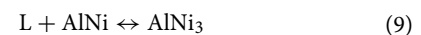
like Al_3Ni or Al_3Ni_2 . Similarly, the IMC-Ni interface is Ni-rich, indicating that Ni-rich IMCs such as $AlNi_3$ or Al_3Ni_5 are likely to form. The elemental distribution across the interfacial IMC layer [Spot 1 and Spot 3 of Fig. 6(a)] suggested that the Al-Ni IMC layer is a combination of $Al_3Ni_2 + AlNi$ IMCs, probably having more of Al_3Ni_2 as it is the most stable form among the Al-Ni IMCs [10]. The formation kinetics of Al_3Ni_2 and $AlNi$ at the Al-Ni interface can be explained by the following reaction [10], in which the molten liquid partially transforms into $AlNi$ IMC first, and then the rest of the liquid transforms into more stable Al_3Ni_2 .



whereas on the Al side, the $Al + Al_3Ni$ type combination is formed by the following reactions [10], which is confirmed by the elemental distribution at Spot 2, as shown in Fig. 6(a).



Similarly, the elemental distribution at Spot 4 [Fig. 6(a)] on the Ni side of the IMC layer indicates the formation of $AlNi_3$, which can be formed by peritectic or eutectic reactions [10].



The line scan of the AN1 sample across the three IMC regions also supports the same observation where the Ni percentage is higher at the IMC-Ni interface and lower at the IMC-Al interface, but nearly equal in proportion with Al at the center of the IMC layer as shown in Fig. 6(b). A schematic representation of the formation of intermetallic regions at the Al-Ni interface is shown in Fig. 6(c). This representation clearly explains the phase formation across the Al-Ni interface developed in WAAM process. Moving from Ni to Al, the IMC phase formation is found in the sequence as $Ni6025 \rightarrow AlNi_3 \rightarrow AlNi + AlNi_3 \rightarrow AlNi \rightarrow AlNi + Al_3Ni \rightarrow Al_3Ni \rightarrow Al4043$. However, it has already been discussed that the $AlNi$ is the first IMC phase to form; therefore, the phase formation kinetics move transverse direction towards Al side and Ni side from the center, as $AlNi_3 \leftarrow AlNi + AlNi_3 \leftarrow AlNi \rightarrow AlNi + Al_3Ni \rightarrow Al_3Ni$. The $AlNi$ IMC appeared in granular form, whereas Al_3Ni appeared as dendritic enveloped by Al matrix. The $AlNi_3$ showed Al band structures enveloped by Ni matrix. However, to ensure the formation of the aforementioned phases at the SS-Ni and Al-Ni interfaces, an X-ray diffraction (XRD) analysis was performed

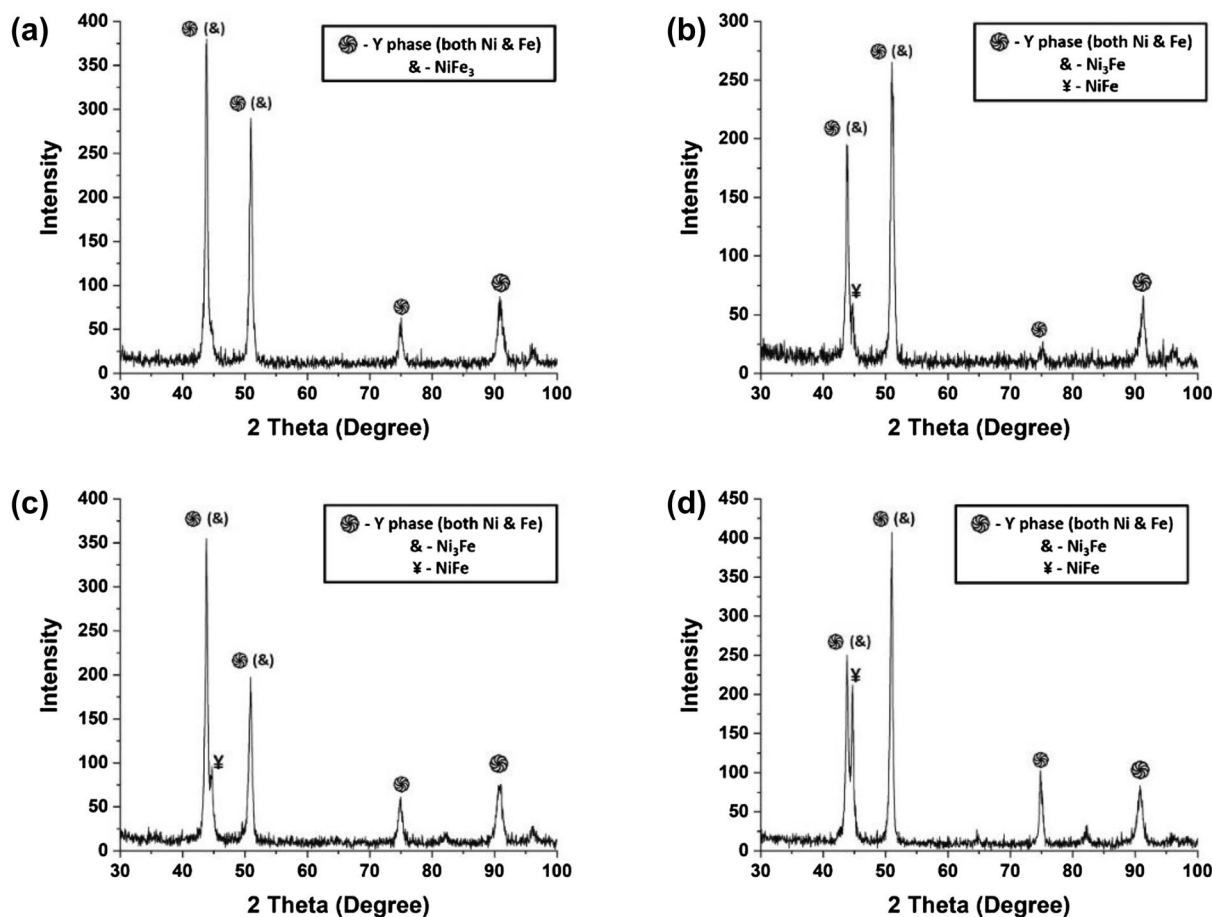


Figure 7: XRD peaks of SS–Ni interface for (a) NS1, (b) NS2, (c) NS3, (d) NS4.

at the specific location and the results are described in the following section.

X-ray diffraction (XRD) analysis

The XRD analysis was also conducted on SS–Ni and Al–Ni interfaces separately to understand and validate the formation of different IMCs in the EDS analysis mentioned in the previous section.

SS–Ni region

The obtained diffraction peaks from SS–Ni interface indicate the presence of austenitic (γ) phase overlapped by the variation of Ni–Fe IMCs in different samples [Fig. 7]. The NS1 sample showed higher γ -phase overlapped with mostly NiFe₃ IMC, as shown in Fig. 7(a). The phases overlap because of their FCC crystal structure (NiFe₃ IMC is a L1₂ FCC structure). It is also difficult to identify the dominating phase between the NiFe₃ and γ -phase from diffraction patterns. But it can be understood that the γ -phase is the matrix phase and NiFe₃ is precipitated at the interface due to the mixing of elements, as discussed in the

previous section [Figs. 2 and 4]. The NS2 and NS3 samples show almost similar phase fractions among each other and the presence of NiFe IMC in both samples. The NS3 sample has a slightly higher NiFe fraction (2%) than the NS2, probably due to higher input associated with the sample. It should be noted here that both NiFe₃ and Ni₃Fe have the same L1₂ crystal structure [10]; hence the diffraction peaks of both phases generally overlap. But the EDS analysis discussed in the previous section confirmed that the NiFe₃ is only observed in the NS1 sample. Thus, the diffraction peaks in other samples must be occurred due to the precipitation of Ni₃Fe IMC. The NS4 sample also shows the formation of Ni₃Fe + NiFe IMCs at the interface similar to NS2 and NS3 samples, but the diffraction peak of NiFe is more prominent than the others. Therefore, it can be stated that the NiFe phase fraction increases from 0 to 19.72% with the increase in heat input from 200 to 670 J/mm.

Al–Ni zone

The XRD analysis of Al–Ni interfaces also confirmed the formation of Al–Ni IMCs, i.e., Al₃Ni, Al₃Ni₂, AlNi, and AlNi₃. The AN1 sample has the lowest heat input (40 J/mm) and IMT; therefore,

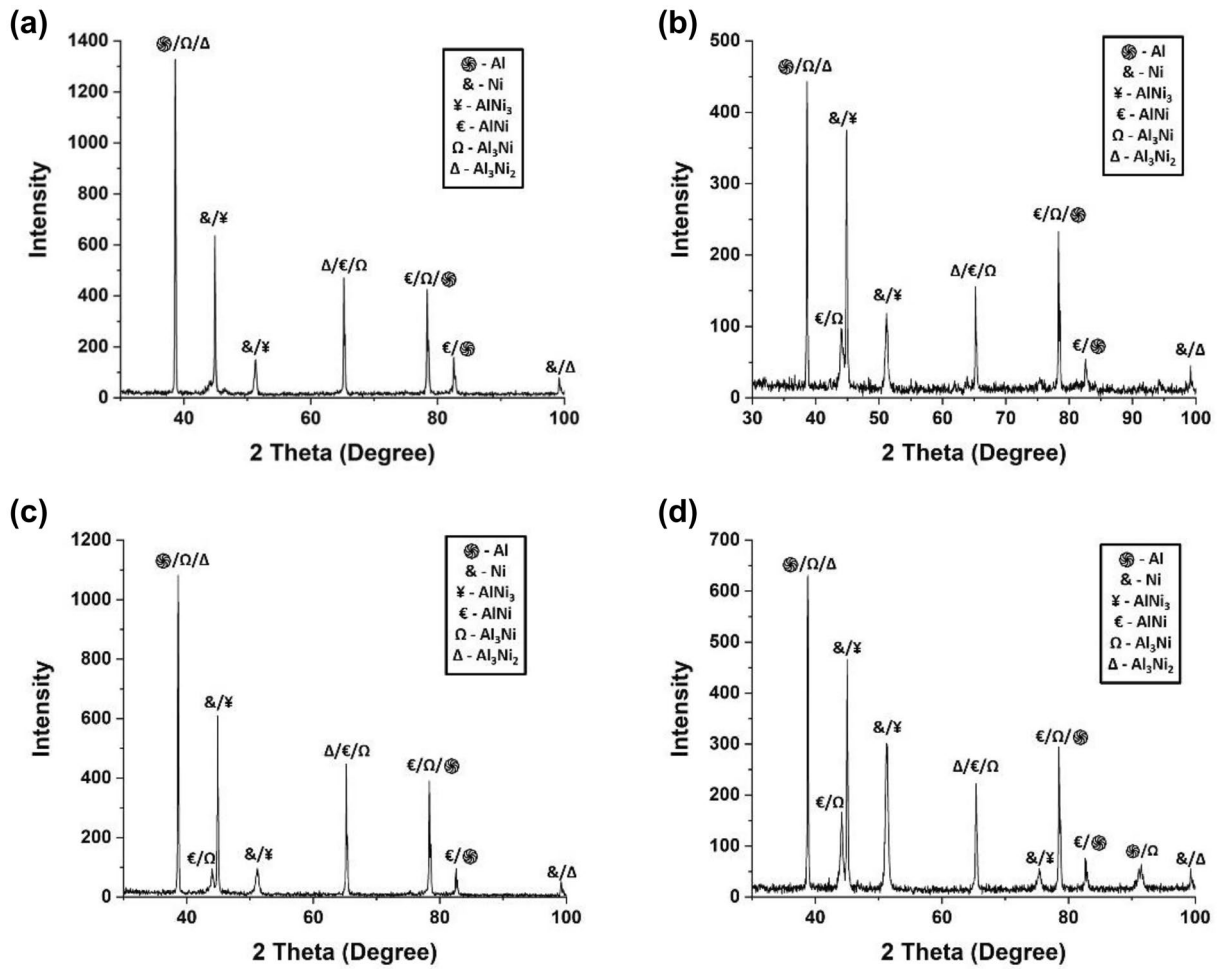


Figure 8: XRD peaks of Al–Ni interface for (a) AN1, (b) AN2, (c) AN3, (d) AN4.

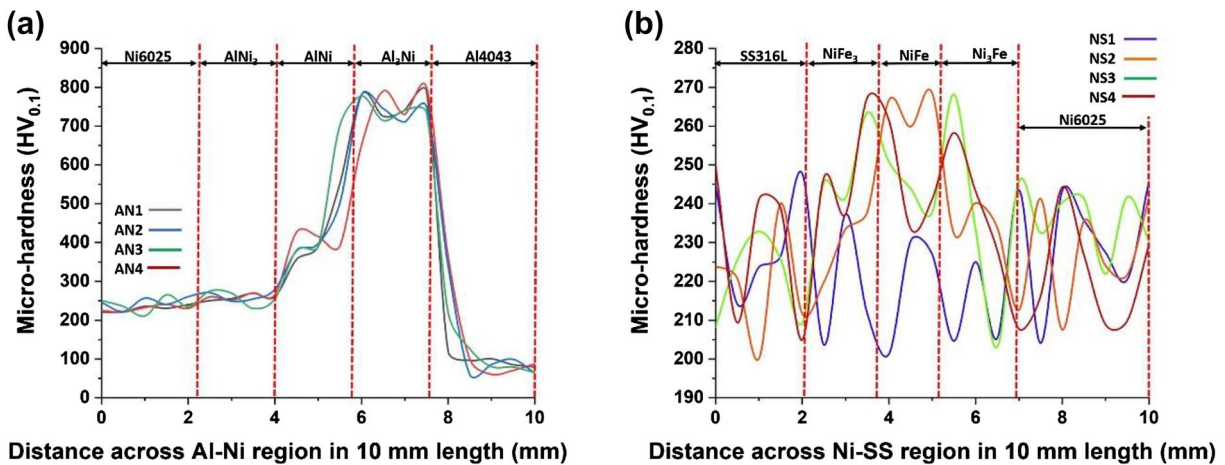


Figure 9: Hardness plot for (a) Al–Ni region, (b) SS–Ni region.

lesser formation of IMCs can be noticed in the diffraction pattern compared to the other samples [Fig. 8(a)]. As the heat input increases from 40 to 65 J/mm (AN2), the peaks of AlNi+Al₃Ni

IMCs increase, justifying the increase of IMT and Al₃Ni IMC. Higher heat input may induce more elements mixing and more Ni penetration in the Al matrix, which also enhances the formation

of Al_3Ni_2 and AlNi_3 , as shown in Fig. 8(b). In the AN3 sample, a higher heat input (70 J/mm) would have increased the phase fraction of $\text{AlNi} + \text{Al}_3\text{Ni} + \text{Al}_3\text{Ni}_2$ IMCs at the interface, as shown in Fig. 8(c). The AN4 sample shows higher diffraction peaks of IMCs with additional intensities of Al_3Ni and AlNi_3 [Fig. 8(d)], justifying the formation of the thickest IMT at the interface [Fig. 4(d)].

Micro-hardness

The micro-hardness was performed along the build direction of the developed wall across the dissimilar interfaces such as the Al–Ni and SS–Ni regions, and the plots are shown in Fig. 9. The plot of micro-hardness for the Al–Ni region [Fig. 9(a)] justifies the respective hardness values of the IMCs formed at the Al–Ni interface. Paul et al. [10] already discussed the crystal structures of the different Al–Ni IMCs; accordingly, they mentioned that Al_3Ni has a D0_{20} crystal structure, AlNi has B2, and AlNi_3 has an L1_2 crystal structure. The L1_2 crystal structure is an FCC-based crystal structure, and therefore, AlNi_3 comes up with lower hardness values, more or less close to the Ni alloy, among the other IMCs formed at the Al–Ni region. The B2 is a body centered cubic (BCC)-based crystal structure, and it is obvious that the hardness value of AlNi is higher than that of AlNi_3 . The Al_3Ni has maximum micro-hardness among the Al–Ni IMCs. The crystal structure of Al_3Ni is a higher derivative of L1_2 (FCC-based crystal structure), despite its maximum hardness value. This anomalous behaviour can be explained by the effect of the Al fraction in the Al–Ni IMCs, as discussed by Paul et al. [10]. The yield strength of Al–Ni IMCs increases abruptly as the Al content increases, which also increases the hardness. Compared to the Al content, a nominal effect of crystal structure will be inherited on micro-hardness. Therefore, Al_3Ni has the highest Al content, which leads to an increase in its yield strength, hardness, and brittleness altogether.

Looking into the SS–Ni region, there are three kinds of Ni–Fe IMCs found in this study, i.e., NiFe_3 , NiFe , and Ni_3Fe with a crystal structure of L1_2 , L1_0 , and L1_2 , respectively [10]. However, all three crystal structures are FCC-based, but the hardness of L1_0 is higher than that of L1_2 . Therefore, in the hardness plot of the SS–Ni region [Fig. 9(b)], the hardness values for Ni6025 , NiFe_3 , and Ni_3Fe are closer to each other in a certain fluctuation with the distance. But, the hardness value of NiFe IMC is slightly higher than the others due to the corresponding crystal structure. Since the NS1 sample consists of Ni–Fe solid solution + NiFe_3 , its hardness is much lower than that of other samples. In the other three samples, such as NS2, NS3 and NS4, NiFe is present, which increases the hardness of the SS–Ni region significantly compared to other available phases.

Conclusions

The present article deals with the Al–Ni and SS–Ni interfacial characteristics of Al4043–Ni6025–SS316L tri-metallic structure. The following conclusions can be drawn from the above study.

- I. The Al–Ni interface is divided into three distinct IMC zones: AlNi in the center, Al_3Ni on the Al side, and AlNi_3 on the Ni side. The AlNi phase is formed by mixing alloying elements in the molten pool. The Al_3Ni IMC is formed by the dendritic growth of Ni in the Al followed by nucleation and growth of Al on the Ni dendrite after mixing. The AlNi_3 IMC may form through a stretching and folding mechanism followed by partial diffusion.
- II. The SS–Ni interface also has NiFe , NiFe_3 , and Ni_3Fe IMCs, but they are mixed and do not show distinct zones like the Al–Ni interface. The formation of different IMCs at the SS–Ni interface is primarily governed by mixing alloying elements in the molten pool during deposition.
- III. The IMCs at the SS–Ni interface are only controlled by heat input. As the heat input increases, so does the fraction of IMCs.
- IV. On the other hand, the IMCs at the Al–Ni interface are affected not only by heat input but also by the PDAS and DGA of the Ni dendrites nearby. When the heat input and DGA are low, and the PDAS is high, the IMT at the Al–Ni interface is lower.
- V. Al_3Ni has the highest hardness value, followed by AlNi and AlNi_3 . The hardness plot of the SS–Ni interface shows that the hardness values for Ni layer, NiFe_3 , and Ni_3Fe are relatively close. However, the hardness value of NiFe is slightly higher than the other IMCs. It is also observed that the hardness of both interfaces increases with increasing heat input.

Experimental procedure

Materials

The SS316L, Ni6025 and Al4043 filler wires of 1.2 mm diameter were selected to develop tri-metallic thin wall structures of 50 mm length and 30 mm height. The SS304L stainless steel plate of 200 mm × 200 mm × 20 mm was used as the substrate for the deposition. The chemical composition of the substrate and other filler materials are shown in supplementary information Table ST5 [23–25].

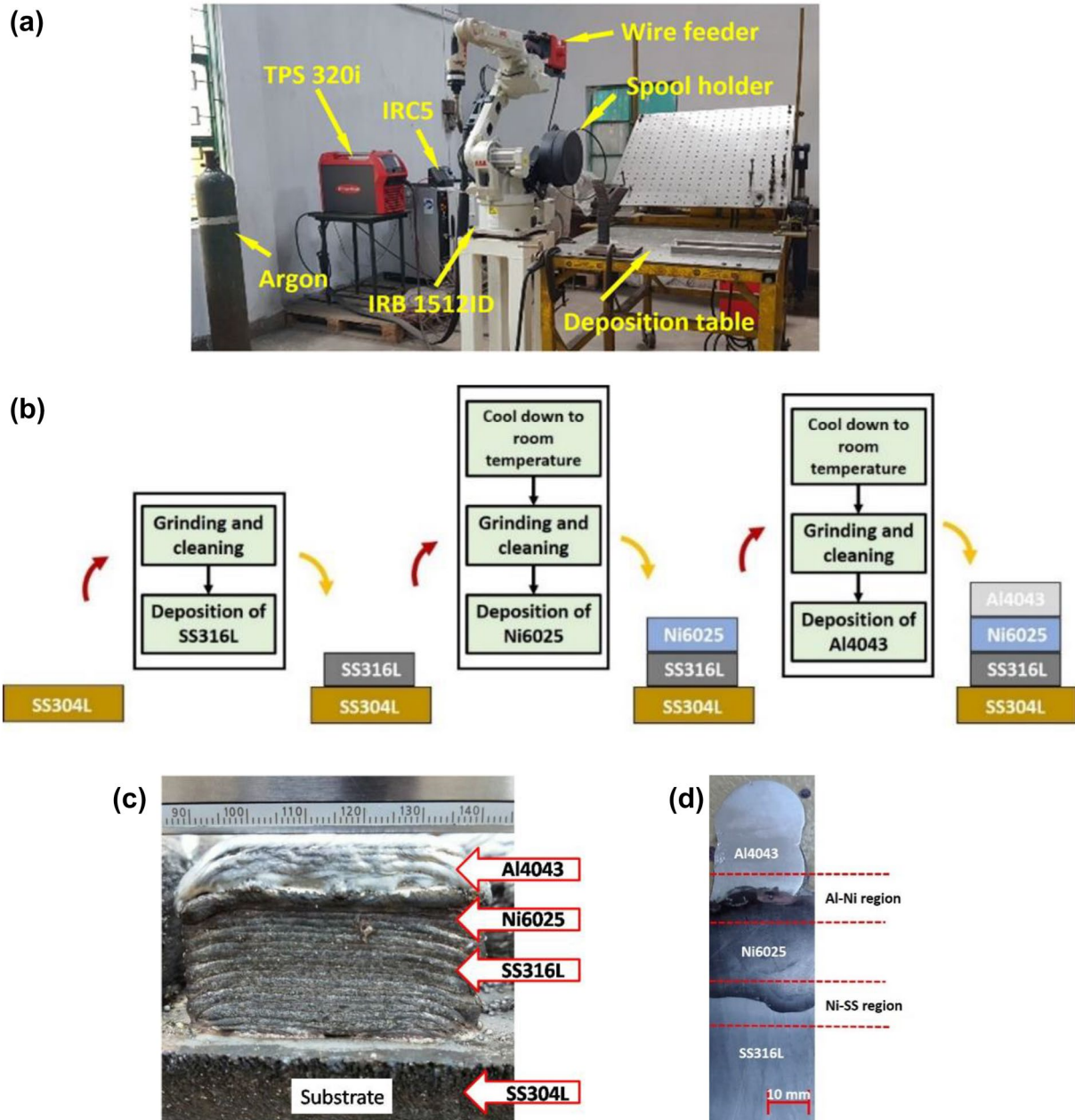


Figure 10: (a) WAAM set-up used for deposition, (b) Schematic diagram of filler sequence during the deposition of wall, (c) A typical as-deposited FGS wall consists of 316L, Ni6025, and Al4043 layers on 304L substrate. (d) Cross-section of the as-deposited wall with marked regions.

Methodology

A 6—degree of freedom articulated robotic arm (ABB1520ID, USA) equipped with the direct energy deposition (DED) power source (Fronius, TPS320i, Austria) were used for the tri-metallic deposition, as shown in Fig. 10(a). Initially, the DoE for Ni and Al alloys was performed using two factors: mean current (I_m) and deposition speed (DS), as well as five levels. In this way 25 walls have been obtained from the DoE. Since, the SS316L was deposited at the base of the wall, it would not affect the SS–Ni interface significantly

as the intermetallic formation at the interface was driven by the deposition parameters of Ni6025. Therefore, the deposition parameters for SS316L was kept at $I_m = 150$ A and $DS = 5$ mm/s, with a constant gas flow rate (GFR) of 19 L/min and a contact tip to workpiece distance (CTWD) of 15–17 mm. The complete parameters for the deposition of Ni6025 and Al4043 during DoE can be seen in supplementary information as Table ST6. The filler sequence used to create the walls are schematically represented in Fig. 10(b). The SS316L was deposited first on the SS304L substrate up to

a height of ~ 15 mm, followed by Ni6025 (up to ~ 5 mm) and Al4043 (up to ~ 10 mm). The 'to be deposit surface' was flattened by grinding operation and cleaned by acetone before the individual material section of the tri-metallic walls was disposed of. The top surface of the deposited SS316L wall was ground and flattened properly before the deposition of Ni6025. The grinding process was performed again on the Ni6025 layer before deposition of Al4043. The deposited structures were also allowed to cool to room temperature before the grinding operation. During the deposition of each material segment, however, the layers were deposited back-to-back with no time delay between two consecutive layers. The as-deposited wall can be seen in Fig. 10(c), and the cross-sectional view of the as-deposited wall is shown in Fig. 10(d). After measuring Al-Ni intermetallic thickness (IMT) and Ni-Fe IMT, through an optical microscope, the four samples were selected based on the increasing thickness of Al-Ni IMC (as it is more crucial than the Ni-Fe IMT formed at SS-Ni interface) in the range of 200 μm to 800 μm with step size 200 μm . In such a way, the sample has Al-Ni IMC ~ 200 μm , ~ 400 μm , ~ 600 μm and ~ 800 μm were chosen for further characterization. Moreover, to better understand the Al-Ni interfacial behaviour, the average grain size (AGS) of Al and primary dendrite arm spacing (PDAS) of Ni was also measured for all 25 walls obtained from the DoE. The complete list of measured output response data can be seen in supplementary information as Table ST1. However, the four selected samples have two important regions, i.e., Al-Ni region and SS-Ni region, as shown in Fig. 10(c); therefore, for better understanding and picturization of the interfacial phenomena, the Al-Ni regions of the selected samples A5, D3, E3, and B1, were renamed as AN1, AN2, AN3, and AN4, respectively, by arranging the samples with increasing order of heat input. The heat input was calculated by using the formula given in Eq. 10 where η represents the arc efficiency, which is taken as 0.85 for the calculation, I_m represents the input current (Ampere), V represents the input voltage (Volts), and DS represents the deposition speed (mm/s). Similarly, the SS-Ni regions of the selected samples, i.e., A5, D3, B1, and E3, were also renamed with increasing order of heat input as NS1, NS2, NS3, and NS4, respectively. The calculated heat input of the Al-Ni and SS-Ni regions, their respective outputs, and their corresponding names are illustrated in Table ST7. It should be noted that parameters of Ni6025 were used to calculate the heat input at the SS-Ni region, and the parameters of Al were used to calculate the heat input at the Al-Ni region.

$$\text{Heat input}(J/\text{mm}) = \frac{\eta \times I_m \times V}{DS} \quad (10)$$

Metallurgical and mechanical characterisation

The selected samples (04 nos.) were analysed by scanning electron microscopy (make—Carl Zeiss, made in Germany, and model—Sigma HD-0112), and pictures of different IMC regions were captured. The area and line scans were performed by energy-dispersive X-ray spectroscopy (EDS) (Oxford's EDS system) were performed nearer to the intermetallic regions (Al-Ni and SS-Ni) and across the regions, respectively. Following the SEM and EDS of various IMC regions, such as the Al-Ni and SS-Ni regions, they were extracted from all four samples for X-ray diffraction (XRD). A Rigaku MiniFlex XRD system with a HyPix-400 MF 2D hybrid pixel array detector (HPAD) and a 600 W X-ray source was used to conduct XRD analysis of as-deposited samples. The phase analysis was performed in SmartLab Studio-II software. The samples were analysed properly at a scan rate of 1°/min in 20° to 100°. The samples were further taken for the Vicker's micro-hardness testing (Model—Anova Falcon 500, Manufacturer—Innovatest). The indentations were taken continuously with a gap of 0.5 mm along the build direction in 10 mm of length across the Al-Ni and SS-Ni regions of the selected samples. During the test 100 gf load was used along with the 10 s of dwell time.

Acknowledgments

The authors would like to acknowledge the DST-SERB for the financial support (Sanction No. ECR/2018/001250) to carry out the research activities. The authors would also like to acknowledge Director, CSIR-CMERI, for providing the opportunity, and facilities to carry out the research work.

Data availability

There is no need for a separate archive since the manuscript contains all the details needed to reproduce the work.

Declarations

Conflict of interest The authors declare that they have no known conflicts of interest that could have influenced the research presented in this paper.

Supplementary Information

The online version contains supplementary material available at <https://doi.org/10.1557/s43578-022-00732-w>.

References

1. A.C.M. Bekker, J.C. Verlinden, G. Galimberti, Challenges in assessing the sustainability of wire + arc additive manufacturing

- for large structures. *Int. Solid Free Fabr. Symp. An Addit. Manuf. Conf. SFF I*, 406–416 (2016)
2. P. Colegrove, High deposition rate high quality metal additive manufacture using wire + arc technology, *Cranf. Univ.* (2010).
 3. A.R. Paul, M. Mukherjee, M. Raja, S. Kundu, A. Chatterjee, Development of near homogeneous properties in wire arc additive manufacturing process for near-net shaped structural component of low-carbon steel. *Proc. Inst. Mech. Eng. Part C* **236**, 3497–3511 (2022)
 4. J. Wanwan, Z. Chaoqun, J. Shuoya, T. Yingtao, W. Daniel, L. Wen, Wire arc additive manufacturing of stainless steels: a review. *Appl. Sci.* **10**, 1563 (2020)
 5. K.S. Derekar, A review of wire arc additive manufacturing and advances in wire arc additive manufacturing of aluminium. *Mater. Sci. Technol.* **34**, 895–916 (2018)
 6. B. Dong, Z. Pan, C. Shen, Y. Ma, H. Li, Fabrication of copper-rich Cu-Al alloy using the wire-arc additive manufacturing process. *Metall. Mater. Trans. B* **48**, 3143–3151 (2017)
 7. F. Veiga, A.G. Del Val, A. Suárez, U. Alonso, Analysis of the machining process of titanium Ti6Al-4V parts manufactured by wire arc additive manufacturing (WAAM). *Materials* **13**, 15 (2020)
 8. R. Karunakaran, S. Ortgies, A. Tamayol, F. Bobaru, M.P. Sealy, Additive manufacturing of magnesium alloys. *Bioact. Mater.* **5**, 44–54 (2020)
 9. X. Xu, J. Ding, S. Ganguly, S. Williams, Investigation of process factors affecting mechanical properties of Inconel 718 superalloy in wire + arc additive manufacture process. *J. Mater. Process. Technol.* **265**, 201–209 (2019)
 10. A.R. Paul, M. Mukherjee, D. Singh, A critical review on the properties of intermetallic compounds and their application in the modern manufacturing. *Cryst. Res. Technol.* **57**, 1–19 (2022)
 11. Y. Tian, J. Shen, S. Hu, J. Gou, E. Kannatey-Asibu, Wire and arc additive manufactured Ti-6Al-4V/Al-625Cu dissimilar alloys by CMT-welding: effect of deposition order on reaction layer. *Sci. Technol. Weld. Join.* **25**, 73–80 (2020)
 12. G. Marinelli, F. Martina, H. Lewtas, D. Hancock, S. Ganguly, S. Williams, Functionally graded structures of refractory metals by wire arc additive manufacturing. *Sci. Technol. Weld. Join.* **24**, 495–503 (2019)
 13. T. Abe, H. Sasahara, Dissimilar metal deposition with a stainless steel and nickel-based alloy using wire and arc-based additive manufacturing. *Precis. Eng.* **45**, 387–395 (2016)
 14. C. Shen, Z. Pan, D. Cuiuri, D. Ding, H. Li, Influences of deposition current and interpass temperature to the Fe3Al-based iron aluminide fabricated using wire-arc additive manufacturing process. *Int. J. Adv. Manuf. Technol.* **88**, 2009–2018 (2017)
 15. G. Sierra, P. Peyre, F.D. Beaume, D. Stuart, G. Fras, Galvanised steel to aluminium joining by laser and GTAW processes. *Mater. Charact.* **59**, 1705–1715 (2008)
 16. Y. Su, X. Hua, Y. Wu, Effect of input current modes on intermetallic layer and mechanical property of aluminum-steel lap joint obtained by gas metal arc welding. *Mater. Sci. Eng. A* **578**, 340–345 (2013)
 17. H.J. Yi, J.W. Kim, Y.L. Kim, S. Shin, Effects of cooling rate on the microstructure and tensile properties of wire-arc additive manufactured Ti-6Al-4V alloy. *Met. Mater. Int.* **26**, 1235–1246 (2020)
 18. O. Grong, *Metallurgical modelling of welding*, 1st edn. (The institute of materials, UK, 1994).
 19. W.D. Callister, *Fundamentals of Materials Science and Engineering: an Integrated Approach*, 6th edn. (Wiley, New York, 2019)
 20. D. Das, D.K. Pratihari, G.G. Roy, Establishing a correlation between residual stress and natural frequency of vibration for electron beam butt weld of AISI 304 stainless steel. *Arab. J. Sci. Eng.* **45**, 5769–5781 (2020)
 21. G. Phanikumar, P. Dutta, K. Chattopadhyay, Continuous welding of Cu-Ni dissimilar couple using CO₂ laser. *Sci. Technol. Weld. Join.* **10**, 158–166 (2005)
 22. K.S. Kumar, G. Phanikumar, P. Dutta, K. Chattopadhyay, Microstructural development of dissimilar weldments: Case of MiG welding of Cu with Fe filler. *J. Mater. Sci.* **37**, 2345–2349 (2002)
 23. M. Mukherjee, T.K. Pal, Evaluation of microstructural and mechanical properties of Fe-16Cr-1Ni-9Mn-012N austenitic stainless steel welded joints. *Mater. Charact.* **131**, 406–424 (2017)
 24. G. Saad, S.A. Fayek, A. Fawzy, H.N. Soliman, G. Mohammed, Deformation characteristics of Al-4043 alloy. *Mater. Sci. Eng. A* **15**, 904–910 (2010)
 25. V.D. ThyssenKrupp, Nicrofer 6025 HT-alloy 602 CA. *Mater. Data Sheet* **4037**, 2–5 (2007)

Springer Nature or its licensor holds exclusive rights to this article under a publishing agreement with the author(s) or other rightsholder(s); author self-archiving of the accepted manuscript version of this article is solely governed by the terms of such publishing agreement and applicable law.